

pubs.acs.org/cm Article

Antiferromagnetic Ordering in Quasi-One-Dimensional FeBi₄S₇

Ian Campbell, Vasile Ovidiu Garlea, Qiang Zhang, Yuwaraj Adhikari, Peng Xiong, Nathan J. Yutronkie, Andrei Rogalev, and Michael Shatruk*



Cite This: Chem. Mater. 2024, 36, 3417-3423



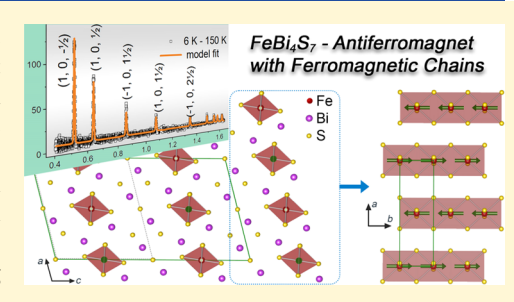
ACCESS I

Metrics & More

Article Recommendations

Supporting Information

ABSTRACT: We report a detailed study of the synthesis, composition, magnetic structure, and transport properties of a quasi-one-dimensional antiferromagnet FeBi₄S₇ that contains chains of edge-sharing FeS₆ octahedra. High-resolution powder X-ray diffraction (PXRD) analysis, aided by variation of synthetic conditions, suggests that the true formula of the material is Fe_{1.2}Bi_{3.8}S₇, due to the minor substitution of Fe into Bi sites. This finding is in agreement with crystal structure refinement from neutron powder diffraction data as well as with the small band gap of 0.23 eV determined from electrical transport measurements. Analysis of the neutron diffraction pattern collected below the antiferromagnetic ordering temperature of 64 K revealed ferromagnetic coupling between the Fe moments in



the chains of FeS₆ octahedra. The overall ordering, however, is antiferromagnetic due to the antiparallel arrangement of moments on neighboring chains. The collinear spin arrangement is described by a k-vector (1, 0, 1/2), which indicates doubling of the unit cell in the c direction and the loss of the C-centering translation as compared to the nuclear cell. The ferromagnetic nature of the sulfide-bridged chains of Fe²⁺ ions in FeBi₄S₇, in contrast to the antiferromagnetic coupling between Fe moments in compounds with similar structural fragments, can be justified by the analysis of metric parameters that characterize the Fe–S bonding in these materials.

■ INTRODUCTION

Materials with chain-like arrangement of magnetic moments can exhibit complex spin textures and nontrivial magnetic excitations, ^{1–3} which render these materials appealing for application in next-generation spintronic devices. ^{4–7} Chains of antiferromagnetically (AFM) coupled spins are of special interest, as the competition between intra- and interchain AFM coupling generally leads to magnetic frustration and noncollinear magnetic ordering that is easily perturbed by external stimuli, such as applied magnetic or electric fields. ^{8–11} In this vein, a number of ternary chalcogenides have been shown to form helimagnetic structures upon AFM ordering. ^{12–18} It is of interest to explore the evolution of such magnetic structures as a function of the transition metal and the separation between the chains.

Compounds $\mathrm{MBi_4S_7}$ (M = Mn, Fe) have been reported as chain antiferromagnets with ordering temperatures (T_N) of 34 and 67 K, respectively, ¹⁹ but their magnetic structures remain unknown. These crystal structures, which form in the low-symmetry space group C2/m, contain chains of edge-sharing $\mathrm{MS_6}$ octahedra that are connected into the three-dimensional (3D) network by vertex-sharing their sulfur atoms with $\mathrm{BiS_6}$ octahedra and $\mathrm{BiS_7}$ distorted monocapped octahedra (Figure 1). Such structural organization is conducive to the formation of noncollinear spin textures. Indeed, incommensurate helimagnetic structures were reported for several AFM-ordered sulfides and selenides $\mathrm{TM_2X_4}$ (T = Mn, Fe; M = Sb, Bi; X = S, Se) that contain chains of chalcogenide-bridged 3d metal ions. ^{12,17,18,20} It is interesting to note, however, that the chains

of edge-sharing MX_6 octahedra seen in the $\mathrm{MBi}_4\mathrm{S}_7$ structures typically are not observed in the structures of other ternary Mn- or Fe-containing chalcogenides. More common structural motifs in such compounds are chains of edge- or vertex-sharing MX_4 tetrahedra. Among Fe-containing chalcogenides with quasi-one-dimensional (quasi-1D) structures, the only well-studied examples containing chains of edge-sharing FeX6 octahedra are FeSb2S4 and FeMo2S4, which exhibit helimagnetic and collinear AFM structures, respectively. 18,25

Given the relative rarity of the chain motif observed in FeBi₄S₇, we became interested in exploring how the magnetic structure of this antiferromagnet might differ from those of the other quasi-1D iron chalcogenides with similar structural fragments. Herein, we report a detailed study of the structural, magnetic, and transport properties of FeBi₄S₇. We demonstrate that the true composition of this material is better described by the formula Fe_{1.2}Bi_{3.8}S₇, due to the partial substitution of Fe for Bi. This nonstoichiometry might explain a substantially lower band gap determined in our transport measurements as compared to the previously reported band gap determined by optical methods. The magnetic structure determination reveals a collinear AFM structure that features FM alignment

Received: January 27, 2024 Revised: March 12, 2024 Accepted: March 13, 2024 Published: March 26, 2024





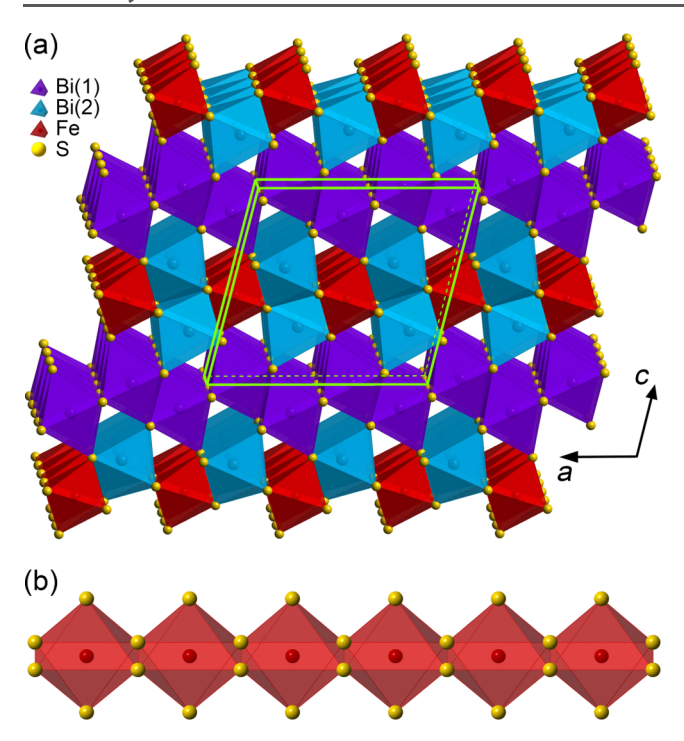


Figure 1. (a) Crystal structure of FeBi₄S₇ viewed approximately down the b axis and showing the chains of edge-sharing FeS₆ octahedra (garnet) connected into the three-dimensional framework by BiS₆ octahedra (teal) and BiS₇ distorted monocapped octahedra (purple). The unit cell is shown with lime-green lines. (b) Side view of a single chain of edge-sharing FeS₆ octahedra.

of Fe magnetic moments along the chains and antiparallel alignment of moments in adjacent chains. We discuss this magnetic structure in light of AFM-ordered spin textures observed in other quasi-1D iron chalcogenides.

MATERIALS AND METHODS

Synthesis. Iron powder (99.9%, Millipore Sigma), bismuth granules (99.997%, Alfa Aesar), and sulfur pieces (99.999%, Alfa Aesar) were used as the starting materials. The Fe powder was additionally purified by heating in a flow of hydrogen gas at 773 K for 5 h, after which the product was stored in an argon-filled dry box (the content of $O_2 < 0.1$ ppm). Mixtures of the constituent elements in the Fe/Bi/S = (1+x):4:7 or (1+x):(4-x):7 ratio (x=0,0.1,0.2), with the total mass of 0.35 g, were sealed under vacuum ($\sim 10^{-4}$ mbar) in fused silica tubes of 10 mm inner diameter (i.d.), with the length of each sealed tube being ~ 10 cm. The tubes with samples were inserted vertically in open alumina crucibles (25 mm i.d.) filled with alumina sand to minimize thermal fluctuations during high-temperature annealing. The samples were placed in a muffle furnace (Thermo Scientific), heated to 923 at 50 K/h, and maintained at this temperature for 5 days, after which they were cooled by air-quenching

to room temperature (r.t.). Importantly, no volatiles were observed in the upper section of the sample tubes, indicating that the thermal gradient was minimal. The products were reground, vacuum-sealed in silica tubes, reannealed at 923 K for 4 days, and air-quenched. The sample for neutron diffraction was prepared in the same way using the stoichiometric ratio of elements, and three such batches were combined to give 1.0 g of the total sample mass.

Powder X-ray Diffraction (PXRD). PXRD was performed at rt on a Panalytical X'Pert Pro diffractometer equipped with an X'Celerator detector and a Cu–K α radiation source (λ = 1.54187 Å). The data were collected in a 2θ range of $10-80^{\circ}$ with a step of 0.05° and the total collection time of 1.5 h. The data analysis was performed with HighScore Plus. To obtain accurate structural parameters and perform Rietveld refinement of PXRD patterns, high-resolution PXRD measurements were performed at rt on beamline 11-BM-B (λ = 0.459059 Å) of the Advanced Photon Source (APS) facility at Argonne National Laboratory. The Rietveld refinement was performed with GSAS-II. The superformed with GSAS-II.

Transport Measurements. Electrical resistance was measured on a powder sample of FeBi_4S_7 that was pelletized by cold-pressing under a pressure of 2000 psi and held for ~ 2 min. The resulting geometrical density was not measured. The measurements were performed on a home-built setup. The current was applied parallel to the flat surface of the pellet, to which platinum wires were attached by means of indium contacts. A 4-probe technique was applied, although 5 indium contacts were used to enable verification of the consistency of results by probing different contact combinations. The DC was applied by means of a Keithley 2400 source meter, while an HP 34401A multimeter was used to measure the voltage. The current bias was chosen and verified to be in the linear region of the I-V curves. The temperature was controlled by a 3 He cryostat (Oxford Cryosystems).

X-ray Absorption Spectroscopy. Fe K-edge X-ray absorption near-edge spectra (XANES) were collected on samples of FeBi $_4$ S $_7$ and reference systems of Fe foil and Fe $_2$ O $_3$ powder using the second harmonic of the Helios-II type undulator at the ID12 beamline (ESRF, The European Synchrotron, Grenoble). All data were recorded at rt using the fluorescence yield detection mode. To eliminate X-ray diffraction peaks from the spectra recorded on FeBi $_4$ S $_7$, we exploited an energy-resolved detector by selecting only Fe K α emission lines. The XANES spectra were normalized using standard procedures and were not corrected for the reabsorption effect.

Neutron Powder Diffraction (NPD). NPD was performed on the time-of-flight neutron diffractometer POWGEN (BL-11A) at the Spallation Neutron Source (SNS) of Oak Ridge National Laboratory (ORNL). Neutron diffraction data were acquired using an incident neutron bandwidth centered at 2.665 and 1.5 Å, at 150 and 7 K. A POWGEN automatic changer (PAC) was used as the sample environment. The powder sample was loaded in a standard vanadium PAC can with a 6 mm diameter and backfilled with helium exchange gas to ensure thermal contact with the PAC temperature stage. Rietveld refinement of the collected data was carried out using FullProf.²⁸ An analysis of symmetry-allowed magnetic models was performed using SARAh representational analysis software²⁹ and the MAXMAGN at the Bilbao Crystallographic Server.³⁰

Table 1. Unit Cell Parameters and the Refined Composition of the Major "FeBi $_4$ S $_7$ " Phase Observed in the High-Resolution PXRD Patterns of the Fe $_{1+x}$ Bi $_4$ S $_7$ and Fe $_{1+x}$ Bi $_{4-x}$ S $_7$ Samples

nominal composition	refined composition	a (Å)	b (Å)	c (Å)	β (deg)	$V(Å^3)$	Bi ₂ S ₃ byproduct (%)
$FeBi_4S_7$ (lit.) ¹⁹	n/a	12.762	3.964	11.804	104.422	578.33	
FeBi ₄ S ₇	$FeBi_4S_7$	12.7211(2)	3.9504(5)	11.7946(5)	104.37(4)	574.19(5)	23 ^a
$Fe_{1.2}Bi_4S_7$	$Fe_{1.15}Bi_{3.85}S_7$	12.7572(3)	3.9616(4)	11.8008(2)	104.48(1)	577.459(2)	22
$Fe_{1.1}Bi_4S_7$	$Fe_{1.11}Bi_{3.89}S_7$	12.7592(9)	3.9627(5)	11.7989(8)	104.41(3)	577.808(1)	11
$Fe_{1.1}Bi_{3.9}S_7$	$Fe_{1.11}Bi_{3.89}S_7$	12.7575(5)	3.9624(4)	11.7990(8)	104.41(3)	577.682(3)	12
$Fe_{1.2}Bi_{3.8}S_7$	$Fe_{1.22}Bi_{3.78}S_7$	12.7543(4)	3.9613(4)	11.8021(9)	104.43(5)	577.481(1)	0

^aThis sample was refined from high-resolution neutron powder diffraction data collected at 150 K (see Table S2).

Magnetic Measurements. Magnetic measurements were performed on a Magnetic Property Measurement System MPMS-3 (Quantum Design) equipped with a superconducting quantum interference device (SQUID). The direct-current (DC) magnetization was measured in the field-cooled regime within the temperature range of 5–300 K, under a variable applied magnetic field. Magnetization isotherms were collected at 6 K, 150 K, and 300 K, with the magnetic field varying from 0 to 70 kOe.

RESULTS AND DISCUSSION

Synthesis and Crystal Structure. Initially, we synthesized FeBi₄ S_7 from a mixture of constituent elements containing a slight excess of iron, which was found to be necessary to suppress the formation of Bi₂ S_3 byproduct in favor of the target ternary phase. Interestingly, however, we observed a decrease in the fraction of the Bi₂ S_3 impurity with increasing Fe excess, which prompted us to explore more carefully the best conditions to achieve a pure phase. To that end, we prepared samples with nominal compositions of Fe_{1+x}Bi₄ S_7 and Fe_{1+x}Bi_{4-x} S_7 , where x = 0, 0.1, and 0.2. In all cases, FeBi₄ S_7 was the major phase, with the lattice parameters in good agreement with previous reports (Table 1). The analysis of high-resolution PXRD data indicated that the composition Fe_{1,2}Bi_{3,8} S_7 produced a single-phase sample (Figure 2), while

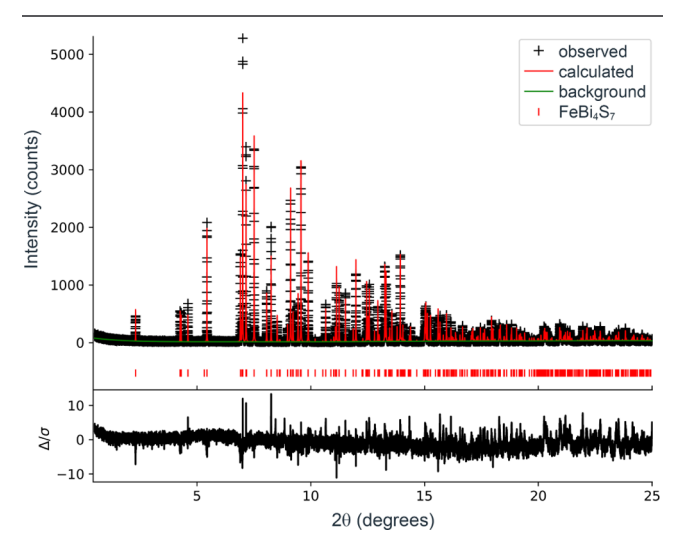


Figure 2. Results of the Rietveld refinement of the high-resolution PXRD patterns of the $Fe_{12}Bi_{38}S_7$ sample.

the nearby compositions, $Fe_{1.1}Bi_{3.9}S_7$, $Fe_{1.1}Bi_4S_7$, and $Fe_{1.2}Bi_4S_7$, still contained the Bi_2S_3 impurity (Figure S1 and Table S1). Thus, we conclude that the composition of the material is better described by the formula $Fe_{1.2}Bi_{3.8}S_7$, which indicates the partial substitution of Fe into Bi sites of the ideal $FeBi_4S_7$ structure. Indeed, it was shown earlier that Fe dopants can substitute for Bi in Bi_2S_3 to give the composition $Bi_{2-x}Fe_xS_3$, up to x=0.26, with the decrease in the unit cell volume caused by the smaller size of the Fe atoms.

The refined unit cell parameters and volume remain nearly constant for all $Fe_{1+x}Bi_4S_7$ and $Fe_{1+x}Bi_{4-x}S_7$ samples, suggesting that the composition of the major phase remains close to that of $Fe_{1.2}Bi_{3.8}S_7$. This notion is also supported by the refined compositions of the major phases for each sample (Table 1). We explored the substitution of Fe for Bi in both Bi(1) and Bi(2) sites, which exhibit, respectively, octahedral and monocapped octahedral coordination by sulfur atoms. These Bi sites correspond to Wyckoff positions 4i (0.62117, 0,

0.9248) and 4i (0.3204, 0, 0.6615), respectively, of the C2/m space group. The Rietveld refinement consistently showed that there is a slight preference for Fe to substitute into the Bi(1) site (Table S1), which can be justified by a better fit of the smaller Fe in the octahedral coordination environment.

The chains of edge-sharing FeS₆ octahedra are characterized by the intrachain Fe···Fe distance of 3.987 Å and the interchain Fe···Fe distance of 6.714 Å. Therefore, in general, magnetic exchange interactions along the chains should be substantially stronger than those between the chains. We will keep this consideration in mind when discussing the magnetic structure of this material in a later section. For the sake of simplicity, we use the stoichiometric formula FeBi₄S₇ in the remaining parts of this paper.

Transport Properties. The temperature dependence of the electrical resistance was measured on a pelletized powder sample of FeBi₄S₇. The resistivity was found equal to \sim 21 Ω · cm at 300 K. This value is substantially higher than 7.1 m Ω ·cm measured by Labégorre et al., 31 who also reported the increase in the resistance with temperature, thus suggesting metallic conductivity for FeBi₄S₇. Such behavior, however, is at odds with the presence of the band gap reported in both previous works on this material. Our transport measurements revealed an exponential increase in the resistance as the temperature was lowered (Figure S2), confirming the semiconducting behavior. Hall measurements were performed to determine the type and density of the majority carriers, revealing n-type conductivity, in agreement with the report by Labégorre et al.³¹ (see Figure S3 and explanation in the Supporting Information).

The dependence of resistivity on inverse temperature (Figure 3) was fit to the Arrhenius law, $\ln(\rho/\rho_o) = E_g/$

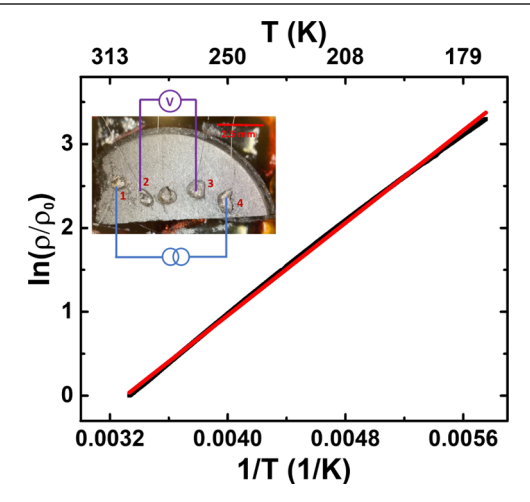


Figure 3. Plot of $\ln(\rho/\rho_0)$ vs 1/T for the pelletized powder sample of FeBi₄S₇. The red line is a linear fit to the Arrhenius law. Inset: an optical image of the sample with a schematic of the 4-probe measurement setup.

 $(2k_{\rm B}T)$, where $\rho_{\rm o}$ is the resistivity at 300 K, $E_{\rm g}$ is the band gap energy, and $k_{\rm B}$ is the Boltzmann constant. The fit to the linear part of the dependence, observed in the high-temperature range, gave $E_{\rm g}=0.23$ eV, which is substantially smaller than the value of 1.30 eV reported by Luo et al. ¹⁹ The latter value, however, was determined from diffuse reflectance data by using the Kubelka–Munk equation, which provides only a very rough approximation to the true band gap. The low value of

the band gap can be justified by the nonstoichiometry observed for our sample. The partial substitution of Fe into the Bi sites, evidenced by the formula $\mathrm{Fe_{1.2}Bi_{3.8}S_7}$ refined from the high-resolution PXRD data of the phase-pure sample, suggests ~5% substitution of $\mathrm{Fe^{3^+}}$ ions in the Bi sites, in addition to the $\mathrm{Fe^{2^+}}$ ions that occupy the main Fe site in the crystal structure (Table S1). Therefore, the lower band gap can be attributed to the mixed valence of Fe, which leads to the appearance of additional states in the vicinity of the Fermi level and the decrease in the E_g value as compared to the values calculated for the pristine $\mathrm{FeBi_4S_7}$.

X-ray Absorption Spectroscopy. The mixed-valence of Fe was investigated by XANES measurements performed on solid samples of FeBi₄S₇ and reference samples of Fe metallic foil and γ -Fe₂O₃ at the Fe K-edge (Figure 4). At first glance,

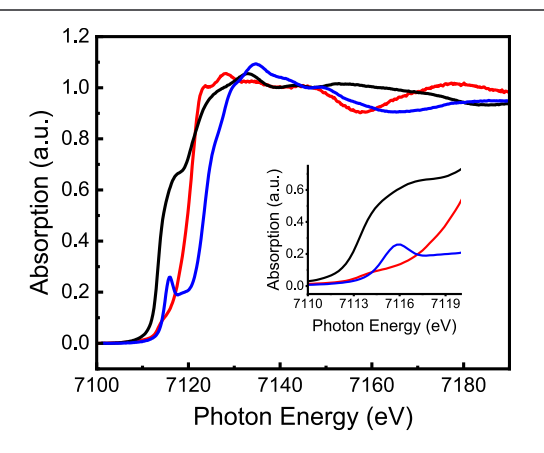


Figure 4. Fe K-edge XANES spectra of FeBi $_4$ S $_7$ (red line) and reference samples of Fe foil (black line) and γ -Fe $_2$ O $_3$ (blue line), with a magnified view of the pre-edge region shown in the inset.

the XANES spectrum of FeBi $_4$ S $_7$ shows a rising edge that falls intermediate in photon energy to Fe metal and γ -Fe $_2$ O $_3$, which may suggest a formal oxidation state of 2+ at the Fe sites of FeBi $_4$ S $_7$. However, the assignment of formal oxidation states becomes more ambiguous upon closer inspection of the preedge region of the spectrum (Figure 4, inset), where $1s \rightarrow 3d$ transitions are typically observed. Here, we observe an apparent lack of a strong pre-edge feature for FeBi $_4$ S $_7$ compared to γ -Fe $_2$ O $_3$. This broad feature, as also observed in the Fe metallic foil, is characteristic of transitions to strongly delocalized 3d states. The observed broadening could also be due to the presence of a mixed-valence system between formally Fe $^{2+}$ ions in the chain-like arrays and the Fe $^{3+}$ ions substituted at the Bi sites.

Macroscopic Magnetic Properties and Magnetic Structure. Magnetization measurements carried out under an applied field of 100 Oe (Figure 5) confirmed the AFM ordering in FeBi₄S₇ at $T_{\rm N}=64$ K. (A small kink observed at 235 K is attributed to a small magnetic impurity that could be present in the powder sample.) The value of the ordering temperature was slightly lower than $T_{\rm N}=67$ K determined by Luo et al.¹⁹ who performed magnetic measurements under an applied field of 5000 Oe. Therefore, we examined the magnetic properties of this material more thoroughly by collecting temperature-dependent magnetization data under a variable applied magnetic field (Figure S4). These measurements revealed that the $T_{\rm N}$ value, indeed, gradually increased with the strength of the applied field (Figure 5, inset). Such a trend is

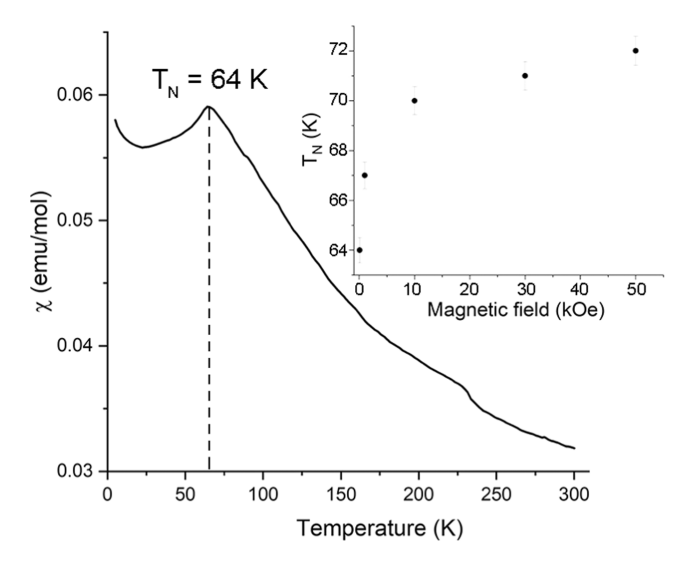


Figure 5. Temperature dependence of magnetic susceptibility of ${\rm FeBi_4S_7}$ under an applied magnetic field of 100 Oe. The inset shows the dependence of the AFM ordering temperature on the applied field.

somewhat counterintuitive because the applied magnetic field typically acts to suppress the AFM ordering, thus decreasing the $T_{\rm N}$ value. These observations suggest that FeBi₄S₇ does not behave as a conventional antiferromagnet. Therefore, we sought to determine its magnetic structure to understand the possible origin of the observed changes in the AFM ordering temperature as a function of the applied magnetic field.

Powder neutron diffraction data were acquired on a POWGEN diffractometer at the ORNL Spallation Neutron Source of the ORNL. The diffraction patterns were recorded above and below $T_{\rm N}$, at 150 and 6 K, respectively (Figure 6). The crystal structure was refined using the 150 K data collected with incident neutron wavelength centered at 1.5 Å. Several unindexed small impurity peaks, not belonging to ${\rm Bi}_2{\rm S}_3$ impurity, remained unidentified and were excluded from refinement. Due to the similar neutron scattering lengths of Fe (9.45 fm) and Bi (8.53 fm), an accurate refinement of the partial Fe substitution into the Bi site was not possible. Nevertheless, the refinement provided accurate determination of the S positions and their occupancies and thermal factors. The final refined parameters are given in Table S2.

The pattern collected at 6 K revealed the appearance of new diffraction peaks in the low-Q region, indicating symmetry breaking due to AFM ordering. The additional reflections observed at 6 K were successfully indexed with a propagation vector $\mathbf{k} = (1, 0, 1/2)$, providing the relationship between the nuclear and magnetic unit cells. The vector $\mathbf{k} = (1, 0, 1/2)$ implies doubling of the unit cell in the c direction and loss of centering in the ab plane, since $\mathbf{m}_i(0,0,0) = -\mathbf{m}_i(0,0,1) = \mathbf{m}_i(0,0,2)$ and $\mathbf{m}_i(0,0,0) = -\mathbf{m}_i(1/2,1/2,0) = \mathbf{m}_i(1,1,0)$, respectively (see the Supporting Information for more details).

There are two possible maximal magnetic space groups, C_c2/c and C_c2/m , allowing magnetic order for the Fe²⁺ ion at the fully occupied Wyckoff position 2c (0,0,1/2). While the first space group constrains the moments to the ac plane, the second allows only their collinear arrangement along the b axis. The neutron data displaying scattering at the (h,0,l+1/2) positions are well described by the C_c2/m space group in a magnetic unit cell defined as $a \times b \times 2c$ with respect to the parent nuclear lattice. The corresponding irreducible repre-

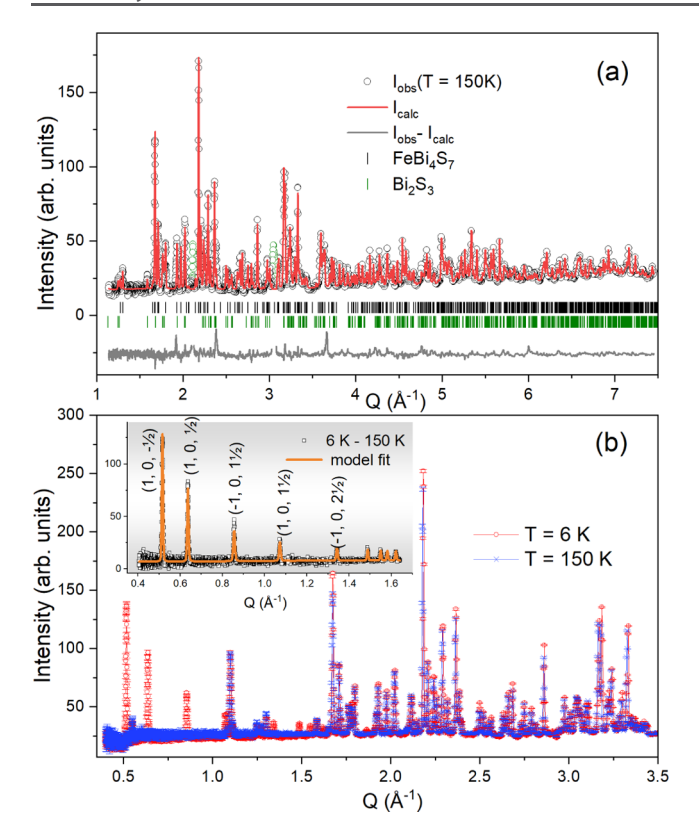


Figure 6. (a) Rietveld refinement of the crystal structure of FeBi₄S₇ using neutron diffraction data collected at 150 K and a wavelength bandwidth centered at 1.5 Å. (b) Comparison of neutron data measured at 6 and 150 K using wavelength bandwidth centered at 2.66 Å. The inset shows a fit of isolated magnetic peaks using the magnetic structure model ($C_c 2/m$ space group), described in the text.

sentation is mM2-.33 The fit of the pure magnetic scattering (Figure 6b, inset), obtained by subtracting the 150 K data from the 6 K data, yields a magnetic R-factor = 3.35% and χ^2 = 1.6. The final refinement of the neutron powder diffraction data at

6 K gave a magnetic moment of 4.39 $\mu_{\rm B}$ per Fe²⁺ parallel to the b axis, in close agreement with the value expected for the S=2

In accordance with the AFM ordering, this magnetic structure reveals an alternating orientation of Fe magnetic moments when moving in the [001] and [110] directions, but not along the [100] or [010] directions (Figure 7). Therefore, the moments are arranged FM along the chains of edge-sharing octahedra parallel to the b axis. The moments in the adjacent chains are arranged in opposite directions, causing the overall AFM order.

The observed magnetic structure allows a plausible explanation for the aforementioned dependence of the AFM ordering temperature on the applied magnetic field (Figure 5, inset). The increasing field should increase the correlation length between the FM-coupled Fe moments along the chains of the FeS₆ octahedra. These longer intrachain FM correlations in the paramagnetic regime should also strengthen the interchain AFM interactions, thus increasing the $T_{\rm N}$ value. (Field-dependent magnetization measurements at 150 and 300 K (Figure S5) reveal essentially linear increase in magnetization, consistent with paramagnetism of the sample in this regime.) The structurally related antiferromagnets, FeSb₂S₄ and FeMo₂S₄, exhibit, respectively, helimagnetic¹⁸ and collinear²⁵ AFM arrangement of Fe moments in the chains of FeS₆ edge-sharing octahedra, in contrast to the FM chains observed in FeBi₄S₇. Therefore, it would be of interest to explore the influence of the applied magnetic field on the AFM ordering temperature for those materials.

To understand the observed differences in the intrachain magnetic exchange in these three compounds, we compare the parameters of Fe–S bonding in their crystal structures (Table 2). In FeBi₄S₇, the separation between the S-bridged Fe atoms is substantially longer and the Fe–S–Fe angle at the sulfide bridge is much larger than those values observed in the structure of FeMo₂S₄. The shorter Fe—Fe separation and more acute Fe–S–Fe angles appear to favor collinear AFM alignment of the Fe moments along the chain. The parameters

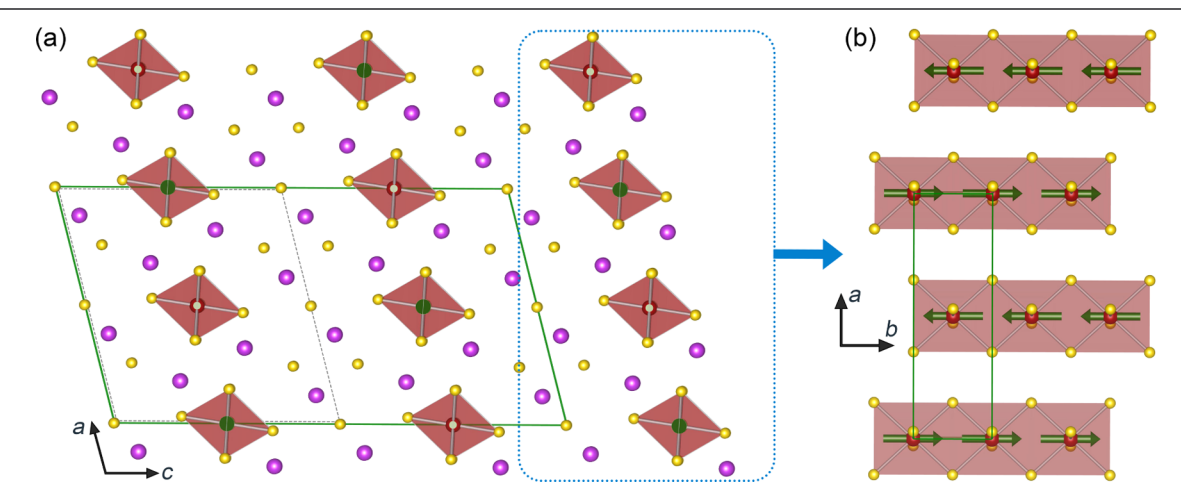


Figure 7. Magnetic structure of FeBi $_4$ S $_7$, with the magnetic and nuclear unit cells indicated with solid green and dashed gray lines, respectively (the nuclear unit cell edges are intentionally displaced for better visibility). (a) The view down the b axis shows the changing orientation of Fe magnetic moments in chains of edge-sharing FeS $_6$ octahedra when moving along the c axis or along the C-centering translation of the monoclinic lattice. The larger dark-green and the smaller light-green dots, which center the octahedra, correspond, respectively, to the "up" and "down" orientations of the Fe magnetic moment vectors. (b) The view down the c axis revealing FM alignment of Fe moments in the chains of edge-sharing FeS $_6$ octahedra, with the antiparallel alignment of the moments in adjacent chains. Such a magnetic structure results in the loss of C-centering translation in the ab plane.

Table 2. Bond Lengths and Bond Angles Observed in the Crystal Structures of FeBi₄S₇, FeSb₂S₄, and FeMo₂S₄

parameter	$\mathrm{FeBi}_{4}\mathrm{S}_{7}$	$FeSb_2S_4$	$FeMo_2S_4$
d(Fe-S), Å	2.700	2.511, 2.618	2.425-2.594
d(Fe···Fe), Å	3.987	3.766	3.189, 3. 377
$\varphi(S-Fe-S)$, deg	84.8	85.4	95.2-100.2
φ (Fe-S-Fe), deg	95.2	92.0, 97.2	79.4-84.0
angle between Fe moments, deg	0	142	180

observed for FeSb₂S₄ lie between those observed for FeBi₄S₇ and FeMo₂S₄, which appears to correlate with the helimagnetic structure of FeSb₂S₄. A similar correlation between the M–X–M angle and the nature of magnetic exchange between the metal centers was reported recently for a series of quasi-1D materials ANiCl₃, where A is an organo-ammonium cation. These materials, which contain chains of face-sharing NiCl₆ octahedra, also showed the change from AFM to FM coupling along the chain of Ni²⁺ ions, with the increase in the Ni···Ni distance and the Ni–Cl–Ni angle.³⁴ It is reasonable to conjecture that the increase in these parameters reduces the strength of the direct M···M exchange and favors FM superexchange across the M–X–M bridges when those exceed certain critical values, depending on the nature of the 3d metal cation and the bridging anion.

CONCLUDING REMARKS

The magnetic structure of FeBi₄S₇ does not follow the more common trend observed for quasi-1D ternary iron chalcogenides, where the collinear AFM or the helical arrangement of moments along the chains is more common. The neutron diffraction analysis clearly reveals the propagation vector k =(1, 0, 1/2), which indicates an AFM alignment of Fe moments in the FM chains that run parallel to the b axis. The AFM ordering temperature slightly increases with the increase in the applied magnetic field, and this trend was observed to hold to a field as high as 50 kOe. Given the relative rarity of chains of edge-sharing FeX₆ octahedra in the known quasi-1D iron chalcogenides, it is certainly of interest to explore the fielddependent magnetic behavior of FeMo₂S₄ and FeSb₂S₄, which contain similar structural fragments. Efforts in this direction are currently underway in our groups. It is also of interest to determine the magnetic structure of the isostructural analogue, MnBi₄S₇. Our preliminary neutron diffraction data indicate that the AFM structure of this material is more complex than that of FeBi₄S₇, and the powder diffraction data are not sufficient for the accurate determination of the corresponding k-vector. Therefore, our future efforts will focus on the growth of large crystals of MnBi₄S₇ to allow the magnetic structure determination from single-crystal neutron diffraction data. The results of all these efforts will be reported in due course.

ASSOCIATED CONTENT

Supporting Information

The Supporting Information is available free of charge at https://pubs.acs.org/doi/10.1021/acs.chemmater.4c00249.

Details of Rietveld refinement of the powder and neutron diffraction data, relationship between the nuclear and magnetic unit cells, additional transport measurement plots, and temperature-dependent magnetic susceptibility measured under variable applied magnetic field (PDF)

AUTHOR INFORMATION

Corresponding Author

Michael Shatruk — Department of Chemistry & Biochemistry, Florida State University, Tallahassee, Florida 32306, United States; National High Magnetic Field Laboratory, Tallahassee, Florida 32310, United States; ocid.org/0000-0002-2883-4694; Email: Email: shatruk@chem.fsu.edu

Authors

Ian Campbell – Department of Chemistry & Biochemistry, Florida State University, Tallahassee, Florida 32306, United States

Vasile Ovidiu Garlea – Neutron Scattering Division, Oak Ridge National Laboratory, Oak Ridge, Tennessee 37831, United States

Qiang Zhang — Neutron Scattering Division, Oak Ridge National Laboratory, Oak Ridge, Tennessee 37831, United States; oorcid.org/0000-0003-0389-7039

Yuwaraj Adhikari – Department of Physics, Florida State University, Tallahassee, Florida 32306, United States

Peng Xiong — Department of Physics, Florida State University, Tallahassee, Florida 32306, United States

Nathan J. Yutronkie – ESRF-The European Synchrotron, Grenoble 38000, France

Andrei Rogalev — ESRF-The European Synchrotron, Grenoble 38000, France

Complete contact information is available at: https://pubs.acs.org/10.1021/acs.chemmater.4c00249

Notes

The authors declare no competing financial interest.

ACKNOWLEDGMENTS

This work was supported by the National Science Foundation (awards DMR-1905499 and DMR-2233902 to M.S. and DMR-1905843 and DMR-2325147 to P.X.). The Quantum Design MPMS-3 system used for magnetic measurements was acquired with support of the NSF MRI program (DMR-2216125). A portion of this research used resources at the Spallation Neutron Source, a U.S. Department of Energy (DOE) Office of Science User Facility operated by the Oak Ridge National Laboratory, and at the Advanced Photon Source, a DOE Office of Science User Facility operated by Argonne National Laboratory under Contract No. DE-AC02-06CH11357. This project also used resources provided by the X-ray Crystallography Center (FSU075000XRAY) and the Materials Characterization Laboratory (FSU075000MAC) at the Department of Chemistry and Biochemistry, Florida State University.

REFERENCES

- (1) Tokura, Y.; Seki, S. Multiferroics with Spiral Spin Orders. *Adv. Mater.* **2010**, 22, 1554–1565.
- (2) Bader, S. D. Magnetism in Low Dimensionality. Surf. Sci. 2002, 500, 172–188.
- (3) Vasiliev, A.; Volkova, O.; Zvereva, E.; Markina, M. Milestones of Low-D Quantum Magnetism. *npj Quantum Mater.* **2018**, 3, No. 18, DOI: 10.1038/s41535-018-0090-7.
- (4) Jungwirth, T.; Marti, X.; Wadley, P.; Wunderlich, J. Antiferromagnetic Spintronics. *Nat. Nanotechnol.* **2016**, *11*, 231–241.

- (5) Baltz, V.; Manchon, A.; Tsoi, M.; Moriyama, T.; Ono, T.; Tserkovnyak, Y. Antiferromagnetic Spintronics. *Rev. Mod. Phys.* **2018**, 90. No. 015005.
- (6) Jiang, N.; Nii, Y.; Arisawa, H.; Saitoh, E.; Onose, Y. Electric Current Control of Spin Helicity in an Itinerant Helimagnet. *Nat. Commun.* **2020**, *11*, No. 1601.
- (7) Tokura, Y.; Kanazawa, N. Magnetic Skyrmion Materials. *Chem. Rev.* **2021**, *121*, 2857–2897.
- (8) Lee, S. H.; Broholm, C.; Ratcliff, W.; Gasparovic, G.; Huang, Q.; Kim, T. H.; Cheong, S. W. Emergent Excitations in a Geometrically Frustrated Magnet. *Nature* **2002**, *418*, 856–858.
- (9) Bordelon, M. M.; Liu, C.; Posthuma, L.; Sarte, P. M.; Butch, N. P.; Pajerowski, D. M.; Banerjee, A.; Balents, L.; Wilson, S. D. Spin Excitations in the Frustrated Triangular Lattice Antiferromagnet NaYbO₂. *Phys. Rev. B* **2020**, *101*, No. 224427.
- (10) Tokura, Y. Multiferroics as Quantum Electromagnets. *Science* **2006**, 312, 1481–1482.
- (11) Ishiwata, S.; Taguchi, Y.; Murakawa, H.; Onose, Y.; Tokura, Y. Low-Magnetic-Field Control of Electric Polarization Vector in a Helimagnet. *Science* **2008**, *319*, 1643–1646.
- (12) Člark, J. K.; Pak, C.; Cao, H.; Shatruk, M. Helimagnetism in MnBi₂Se₄ Driven by Spin-Frustrating Interactions between Antiferromagnetic Chains. *Crystals* **2021**, *11*, No. 242, DOI: 10.3390/cryst11030242.
- (13) Bhutani, A.; Behera, P.; McAuliffe, R. D.; Cao, H.; Huq, A.; Kirkham, M. J.; dela Cruz, C. R.; Woods, T.; Shoemaker, D. P. Incommensurate Magnetism in $K_2 mns_{2-X}se_x$ and Prospects for Tunable Frustration in a Triangular Lattice of Pseudo-1D Spin Chains. *Phys. Rev. Mater.* **2019**, 3, No. 064404.
- (14) Glinka, C. J.; Minkiewicz, V. J.; Cox, D. E.; Khattak, C. P.et al. In *The Magnetic Structure of RbMnBr3*, AIP Conference Proceedings; AIP Publishing, 1973; pp 659–663.
- (15) Eibschütz, M.; Sherwood, R. C.; Hsu, F. S. L.; Cox, C. E. et al. In *Magnetic Ordering of the Linear Chain Antiferromagnet CsMnBr3*, AIP Conference Proceedings; AIP Publishing, 1973; pp 684–688.
- (16) Zandbergen, H. W. Neutron Powder Diffraction and Magnetic Measurements on CsMnI₃. *J. Solid State Chem.* **1980**, *35*, 367–375.
- (17) Léone, P.; Doussier-Brochard, C.; André, G.; Moëlo, Y. Magnetic Properties and Neutron Diffraction Study of Two Manganese Sulfosalts: Monoclinic MnSb₂S₄ and Benavidesite (MnPb₄Sb₆S₁₄). *Phys. Chem. Miner.* **2008**, 35, 201–206.
- (18) Wintenberger, M.; André, G. Magnetic Structure of the Mineral Berthierite FeSb₂S₄. Phys. B: Condens. Matter 1989, 156–157, 315–317
- (19) Luo, Z.-Z.; Lin, C.-S.; Cheng, W.-D.; Zhang, W.-L.; Li, Y.-B.; Yang, Y.; Zhang, H.; He, Z.-Z. From One-Dimensional Linear Chain to Two-Dimensional Layered Chalcogenides XBi₄S₇ (X = Mn, Fe): Syntheses, Crystal and Electronic Structures, and Physical Properties. *Cryst. Growth Des.* **2013**, *13*, 4118–4124.
- (20) Shanbhag, P. N.; Orlandi, F.; Manuel, P.; Etter, M.; Bhat, S.; Sundaresan, A. Successive Ferroelectric Transitions Induced by Complex Spin Structures in MnBi₂S₄. *Phys. Rev. B* **2024**, *109*, No. 024401.
- (21) Tiwary, S. K.; Vasudevan, S. Single Crystal Magnetic Susceptibility of the Quasi-One-Dimensional Antiferromagnet KFeS₂. *Solid State Commun.* **1997**, *101*, 449–452.
- (22) Welz, D.; Deppe, P.; Schaefer, W.; Sabrowsky, H.; Rosenberg, M. Magnetism of Iron-Sulfur Tetrahedral Frameworks in Compounds with Thallium I. Chain Structures. *J. Phys. Chem. Solids* **1989**, *50*, 297–308.
- (23) Zhang, Y.; Lin, L.-F.; Alvarez, G.; Moreo, A.; Dagotto, E. Magnetic States of the Quasi-One-Dimensional Iron Chalcogenide Ba₂FeS₃. *Phys. Rev. B* **2021**, *104*, No. 125122.
- (24) Swinnea, J. S.; Steinfink, H. Mössbauer Spectra, Magnetic and Electrical Behavior of Ba_{1+x}Fe₂S₄ Phases. *J. Solid State Chem.* **1982**, 41, 124–131
- (25) Vaqueiro, P.; Kosidowski, M. L.; Powell, A. V. Structural Distortions of the Metal Dichalcogenide Units in AMo_2S_4 (A = V, Cr,

- Fe, Co) and Magnetic and Electrical Properties. Chem. Mater. 2002, 14, 1201–1209.
- (26) X'pert Highscore Plus Software V. 2.2b; PANalytical B.V.: Almelo, Netherlands, 2006.
- (27) Toby, B. H.; Von Dreele, R. B. GSAS-II: The Genesis of a Modern Open-Source All Purpose Crystallography Software Package. *J. Appl. Crystallogr.* **2013**, *46*, 544–549.
- (28) Rodríguez-Carvajal, J. Recent Advances in Magnetic-Structure Determination by Neutron Powder Diffraction. *Phys. B: Condens. Matter* **1993**, *192*, 55–69.
- (29) Wills, A. S. A New Protocol for the Determination of Magnetic Structures Using Simulated Annealing and Representational Analysis (SARAh). *Phys. B: Condens. Matter* **2000**, 276–278, 680–681.
- (30) Perez-Mato, J. M.; Gallego, S. V.; Tasci, E. S.; Elcoro, L.; de la Flor, G.; Aroyo, M. I. Symmetry-Based Computational Tools for Magnetic Crystallography. *Annu. Rev. Mater. Res.* **2015**, 45, 217–248.
- (31) Labégorre, J.; Virfeu, A.; Bourhim, A.; Willeman, H.; Barbier, T.; Appert, F.; Juraszek, J.; Malaman, B.; Huguenot, A.; Gautier, R.; Nassif, V.; Lemoine, P.; Prestipino, C.; Elkaim, E.; Pautrot-d'Alençon, L.; Le Mercier, T.; Maignan, A.; Al Rahal Al Orabi, R.; Guilmeau, E. XBi_4S_7 (X = Mn, Fe): New Cost-Efficient Layered n-Type Thermoelectric Sulfides with Ultralow Thermal Conductivity. Adv. Funct. Mater. 2019, 29, No. 1904112.
- (32) Silva, R. S.; Mikhail, H. D.; Guimarães, E. V.; Gonçalves, E. R.; Cano, N. F.; Dantas, N. O. Synthesis and Study of Fe-Doped Bi₂S₃ Semimagnetic Nanocrystals Embedded in a Glass Matrix. *Molecules* **2017**, 22, No. 1142, DOI: 10.3390/molecules22071142.
- (33) Cracknell, A. P.; Davies, B. L.; Miller, S. C. Kronecker Product Tables. Vol. 1. General Introduction and Tables of Irreducible Representations of Space Groups; IFI/Plenum: New York, 1979.
- (34) Lee, T.; Straus, D. B.; Devlin, K. P.; Gui, X.; Louka, P.; Xie, W.; Cava, R. J. Antiferromagnetic to Ferromagnetic Coupling Crossover in Hybrid Nickel Chain Perovskites. *Inorg. Chem.* **2022**, *61*, 10486–10492.